1

DROP GENERATION IN CONTROLLED FLUID FLOWS

ELENA CASTRO HERNANDEZ[1], JOSEFA GUERRERO[2], ALBERTO FERNANDEZ-NIEVES[2], & JOSE M. GORDILLO[1]

[1]*Departamento de Ingenieria Aeroespacial y Mecanica de Fluidos, University of Sevilla, Sevillam 41092, Spain*
[2]*School of Physics, Georgia Institute of Technology, Atlanta, GA 30332, USA*

1.1 INTRODUCTION

Drops are present in our everyday life in kitchens and showers and are also used in fountains for aesthetic reasons. In addition, drops are of fundamental importance in many industrial processes [1–6]. Chemical and metallurgical engineers rely on drop formation for operations as varied as distillation, absorption, flotation, and spray drying [7]. Mechanical engineers have studied droplet behavior in connection with combustion operations [6]. In the food industry they are used to mask flavors and change textures [8, 9], and in the pharmaceutical sector they are involved in the production of creams and syrups [10–12].

The most common devices for mass production of drops are mixers and ultrasound emulsificators. In the case of mixers, the breakup of the dispersed phase results from the turbulent motion induced by the mobile parts of the mixer [13], whereas the operation of an ultrasound emulsificator relies on the collapse of cavitation bubbles, which induces velocity gradients in the continuous phase that cause formation of jets and subsequent breakup [14]. These methods are simple, robust, and of low cost, but they typically result in a wide size distribution and a poor control on drop size. These drawbacks can be overcome by filtering the droplets [15, 16]. However, the need of this second step complicates the process and increases costs.

In the last decades, great efforts have been made to improve current production methods in order to obtain monodisperse micron-sized droplets at high production rates. Recent fabrication methods rely on microfluidics as this technology provides great control over fluid flow and mixing of components.

In general, two different regimes can be experimentally observed depending on the operating conditions: dripping and jetting. The dripping regime operates at low flow rates and drop formation occurs right at the exit of the injection tube. In this regime, the resulting droplets are very monodisperse, but the production frequency is low.

Fluids, Colloids and Soft Materials: An Introduction to Soft Matter Physics, First Edition. Edited by Alberto Fernandez Nieves and Antonio Manuel Puertas.

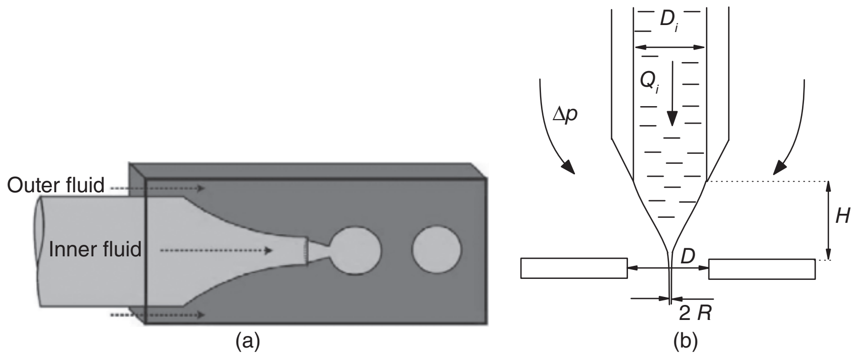

Figure 1.1 (a) Schematic of the coflowing configuration. Source: Reprinted Figure 2a with permission from Ref. [20]. (b) Schematic of the axisymmetric flow focusing configuration. Source: Reprinted Figure 1 from Ref. [52].

In addition, the droplet size is proportional to the diameter of the injection tube, and as a consequence, in order to obtain droplets that are smaller than ∼10 μm, needles with such a small diameter are required. However, in this case, clogging becomes an issue. The jetting regime operates at higher flow rates than the dripping regime. In this case, the drop diameter is proportional to the diameter of the jet, which under the right conditions can be much smaller than the diameter of the injection tube. Jetting can only be achieved under the action of a force field. If only hydrodynamic forces act on the liquid, jetting can be obtained in either the coflow or the flow focusing configurations. Another alternative is the use of electric forces, with techniques such as electrospray (see Chapter 2).

The coflow configuration is characterized by the coaxial flow of two immiscible fluids as shown in Figure 1.1a. In this case, jetting occurs when the tangential stresses exerted by the continuous phase on the dispersed phase overcome surface tension stresses. In flow focusing, two fluids are forced to flow through a small orifice located in front of an injection tube, as shown in Figure 1.1b. In this configuration, the outer pressure gradient is favorable, and, as a consequence, not only the outer tangential stresses but also the outer pressure gradient imposed by the geometry accelerates the inner fluid through the orifice inducing formation of a jet that can be much smaller than the injection tube.

Other emulsification schemes besides coflow and flow focusing, which is the focus of this chapter, have also been explored. An important example is the T-junction geometry introduced by Garstecki *et al.* [19], where an inlet channel containing the dispersed phase perpendicularly intersects the main channel hosting the continuous phase [20] (see Figure 1.2a). Both phases form an interface at the junction, and as the fluid flow continues, the tip of the dispersed phase enters the main channel. The shear stresses of the continuous phase and the subsequent pressure gradient cause the head of the dispersed phase to elongate into the main channel until breakup occurs and a drop is formed, as shown in Figure 1.2b. The size of the drop can be changed by altering the flow rates, the channel dimensions, and the viscosity ratio of the two liquids. This geometry is very popular due to its simplicity and flexibility [21]. The main disadvantage is that the minimum size of the drops is limited by the size of the channel. Despite the production rate is not very high, parallel production can reduce this limitation.

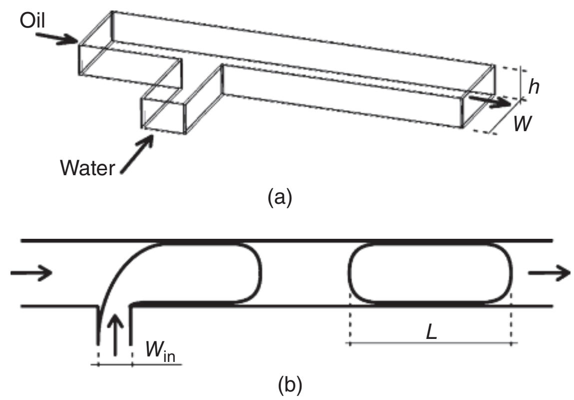

Figure 1.2 (a) Schematic illustration of the microfluidic T-junction composed of rectangular channels. (b) Top view of the same schematic in a two-dimensional representation. Source: Reprinted Figure 1 from Ref. [17].

1.2 COFLOW

1.2.1 Problem and Dimensionless Numbers

One of the simplest designs of a coflow device consists in coaxially aligning two capillary tubes. Typically, the inner one is cylindrical, with a tapered tip, and the outer tube has a square cross section [17]. Coaxial alignment is achieved by matching the outer diameter of the untapered portion of the inner capillary to the inner dimension of the square cross section of the outer tube (Figure 1.1a). As the length scales are below the capillary length, the effects of gravity are negligible. In addition, even if the flow in the outer capillary is not axisymmetric, since the tip is centered in the square cross section and $D_i \ll D_o$, with D_i the inner diameter of the tip and D_o the inner length of the square cross section of the outer capillary, the local flow around the tip is approximately axisymmetric. The inner fluid is injected through the cylindrical capillary tube at a flow rate Q_i and the outer fluid is supplied through the voids between the cross sections of both tubes at a flow rate Q_o.

Drop formation in a coflow device is characterized by nine physical parameters: the densities of both fluids, ρ_i and ρ_o, their viscosities, μ_i and μ_o, their flow rates, the surface tension between the two fluids, σ, the inner diameter of the injection tube, and the inner length of the square cross section of the outer tube. Since there are three fundamental quantities (mass, length, and time), there are $9 - 3 = 6$ independent dimensionless groups [22, 23]. Assuming that the outer viscous stresses are the most relevant stresses in the problem, the selection of μ_o, D_i, and $Q_o = U_o D_o^2$, where U_o is the mean velocity of the outer stream, as characteristic quantities leads to the following six dimensionless parameters:

$$\frac{D_o}{D_i},\ \ q = \frac{Q_i}{Q_o},\ \ \frac{\mu_i}{\mu_o},\ \ Ca_o = \frac{\mu_o U_o}{\sigma},\ \ Re_o = \frac{\rho_o U_o D_i}{\mu_o},\ \ Re_i = \frac{\rho_i U_i D_i}{\mu_i}$$

where Ca_o is the capillary number of the outer fluid, Re_i is the Reynolds number of the inner fluid and Re_o that of the outer fluid in the scale of the tip diameter.

Generally, for low values of the inner to outer flow rate ratio, the dripping regime is observed, whereas for higher values of q, jetting occurs. The inner to outer viscosity ratio, μ_i/μ_o, must play a significant role in the jet formation process, since gas ligaments have not been reported in a coflow configuration at low Reynolds numbers. The inner to outer length ratio, D_i/D_o, is fixed for each device and should be sufficiently smaller than one to avoid wall effects. The rest of the parameters measure the relative importance between different forces in the problem: capillary forces, viscous forces, and inertial forces. The outer capillary number characterizes the relative importance of the outer viscous stress compared to the surface tension stress, while the Reynolds numbers express the ratio between inertial and viscous forces.

Other dimensionless parameters that will appear in the discussion are the inner capillary number, $Ca_i = \mu_i U_i/\sigma$ and the inner Weber number, $We_i = \rho_i U_i^2 D_i/\sigma$; the latter determines the relative importance between inertial and surface tension forces for the inner fluid, with $U_i = 4Q_i/(\pi D_i^2)$ the mean velocity of the inner stream. The inner Ohnesorge number, $Oh_i = \mu_i/(\rho_i v_c D_i)$ will also play a significant role; it measures the importance of inner viscous forces in the development of capillary instabilities, where $v_c = [\sigma/(\rho_i D_i)]^{1/2}$ is the capillary velocity. Note that these numbers can be obtained from combinations of the above-mentioned six parameters.

For given values of the physical parameters in the problem, the magnitude of the dimensionless groups allows identification of the most relevant forces and hence of the expected operating regime of the device.

1.2.2 Dripping and Jetting

When a liquid is forced through an orifice in the presence of a coflowing, immiscible fluid, it can drip or form a jet, depending on the flow rates. In dripping, the growing droplet experiences a force due to the viscous drag exerted by the coflowing fluid and a force due to surface tension, which keeps the drop at the tip of the capillary tube (Figure 1.3a). As the outer flow rate increases, the drop size concomitantly decreases until a critical value of $Ca_o \sim O(1)$ is reached [24]. At this point, the dripping regime transitions into a jetting regime, where a long jet, which narrows in the downstream direction, is formed. This jet ultimately breaks into drops due to the Rayleigh–Plateau instability (Figure 1.3b) [25, 26].

Jetting can also result if the kinetic energy due to the flow of the inner stream at the jet interface overcomes the surface tension energy. In this case, a widening jet results, as shown in Figure 1.3c. Dripping can thus transition into jetting when $We_i > 1$, provided Re_i is also larger than one. These jets are very different from the narrowing jets not only in their shape. The breakup is also very different. In fact, drop formation from these widening jets is reminiscent of dripping at the tip, even if the process takes place a distance downstream of it.

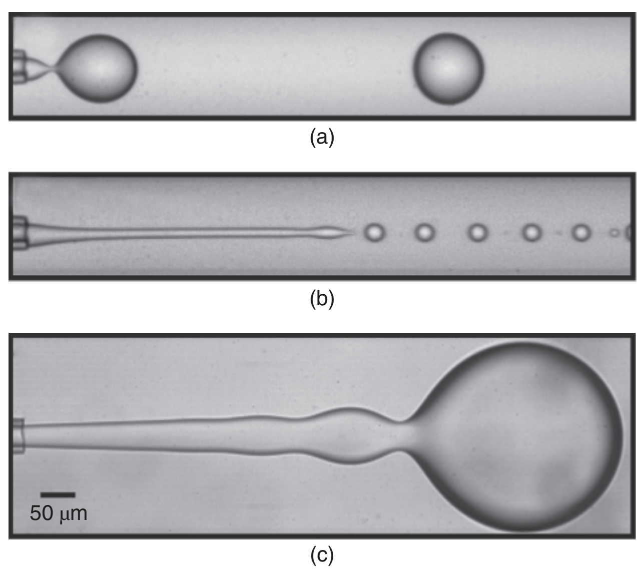

Figure 1.3 Images in the (a) dripping, (b) narrowing jet, and (c) widening jet regimes. Source: Reprinted Figure 1 from Ref. [23]. Copyright 2007 by the American Physical Society.

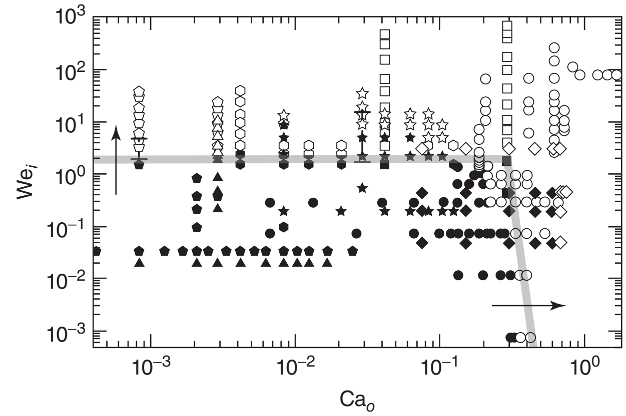

Figure 1.4 State diagram of the dripping-to-jetting transition for coflowing streams as a function of Ca_o and We_i. Filled symbols represent dripping while open symbols represent jetting. Each shape is a different viscosity ratio, surface tension, or geometry. Surface tension is $\sigma = 40$ mN/m unless otherwise stated. Square: $\mu_i/\mu_o = 0.01$. Diamond: $\mu_i/\mu_o = 0.01$, with the extra capillary tube to increase U_o. Hexagon: $\mu_i/\mu_o = 0.1$. Circle: $\mu_i/\mu_o = 0.1$. Pentagon: $\mu_i/\mu_o = 1$. Triangle: $\mu_i/\mu_o = 10$. Star: $\mu_i/\mu_o = 10$ and $\sigma = 4$ mN/m. Source: Reprinted Figure 4 from Ref. [23]. Copyright 2007 by the American Physical Society.

For $Re_o \ll 1$ and $Re_i > 1$, Utada *et al.* [24] proposed a state diagram for the dripping to jetting transition in terms of We_i and Ca_o. For $We_i < 1$, jetting occurs if the outer viscous forces overcome capillary forces, $Ca_o \gg O(1)$, whereas for $Ca_o < 1$, jetting is observed when the inertial forces of the inner liquid dominate over surface tension forces, $We_i > 1$ (Figure 1.4).

More recently, Castro-Hernández *et al.* [27] reported that when $Re_i < 1$, the inner Weber number no longer predicts the transition from dripping to jetting. In this case, the appropriate dimensionless group is the capillary number of the inner fluid; jetting occurs when $Ca_i > 1$.

1.2.3 Narrowing Jets

In this regime, the jet thins downstream until, eventually, its diameter reaches a nearly constant value, as shown in Figure 1.3b. For these jets, when the outer flow rate is increased for a fixed value of the inner flow rate, the jet diameter decreases, whereas when the inner flow rate is increased, for a fixed value of the outer flow rate, the jet diameter increases. The drop size mimics this behavior, as shown in Figure 1.5. Utada *et al.* [28] proposed a simple model to predict the jet diameter for these jets in the axisymmetric coflow configuration. Solving the motion of two coaxial liquids in Stokes flow, $\nabla P = \mu\nabla^2 u$, and relating the mean velocities of both fluids to the flow rates, one obtains

$$\frac{Q_i}{Q_o} = \frac{\mu_o}{\mu_i}\frac{\epsilon^4}{(1-\epsilon^2)^2} + 2\frac{\epsilon^2}{1-\epsilon^2}, \tag{1.1}$$

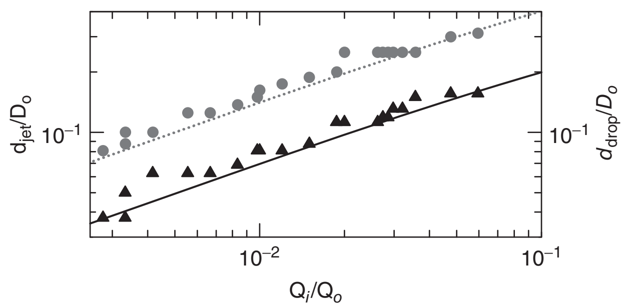

Figure 1.5 Experimentally measured jet diameter (triangles) and droplet diameter (circles) scaled by D_o as a function of the inner to outer flow rate ratio for a viscosity ratio $\mu_i/\mu_o = 0.1$ ($Oh_i = 0.11$). The solid line is the prediction from the model for d_{jet} with no fitting parameters. The dashed line is the predicted result assuming $d_{\text{drop}} \approx 2d_{\text{jet}}$ from the Rayleigh–Plateau instability. Source: Reprinted Figure 2 from Ref. [23]. Copyright 2007 by the American Physical Society.

where $\epsilon = d_{\text{jet}}/D_o$ is the ratio between the diameter of the jet and the inner radius of the outer tube. When $\epsilon \ll 1$ the leading term in Equation 1.1 results in a normalized jet diameter, $d_{\text{jet}}/D_o = \sqrt{Q_i/2Q_o}$, which correctly accounts for the measurements, as shown in Figure 1.5.

The observed proportionality between d_{jet} and the drop size can be understood by considering the Rayleigh–Plateau breakup of a jet, which predicts that the wavelength of the fastest unstable mode, λ^*, is proportional to the jet diameter. The proportionality constant is only a function of the viscosity ratio for sufficiently large Oh_i [29]. Considering that this mode causes the breakup of the jet, we equate the volume of a cylinder of length λ^*, to the volume of the resulting spherical droplet: $\pi d^3_{\text{drop}}/6 = \pi d^2_{\text{jet}}\lambda^*/4$, with d_{drop} the drop diameter. This suggests that the drop size should be proportional to the jet diameter, consistent with the experimental results. In addition, since $\mu_i/\mu_o = 0.1$ and $\lambda^* = 5.48d_{\text{jet}}$, $d_{\text{drop}} \approx 2d_{\text{jet}}$, consistent also with the experimental results (Figure 1.5).

Interestingly, Suryo and Basaran [30] found out numerically that in this coflow geometry, d_{jet} can be much smaller than D_i. Soon after, Marín *et al.* [31] showed that under the right operating conditions, droplets below the micron could be obtained from needles with $D_i = 100$ μm. The requirements for the observation of this regime are that (i) $Re_o \ll 1$, so that the outer flow remains attached at the jet interface, (ii) $Re_i \ll 1$, so that the momentum of the outer fluid effectively diffuses to the inner stream, and (iii) $Ca_o \gtrsim O(1)$. In this case, if $q \ll 1$, a cone-jet transition is observed and the jet diameter can be much smaller than D_i.

Recently, Castro-Hernández *et al.* [32] have studied the role of μ_i/μ_o, Ca_o and q in the coflow configuration when operated under the narrowing-jet regime. They experimentally observed that when the inner to outer flow rate decreases, for fixed values of the viscosity ratio and the outer capillary number, the diameter of the jet and of the droplets

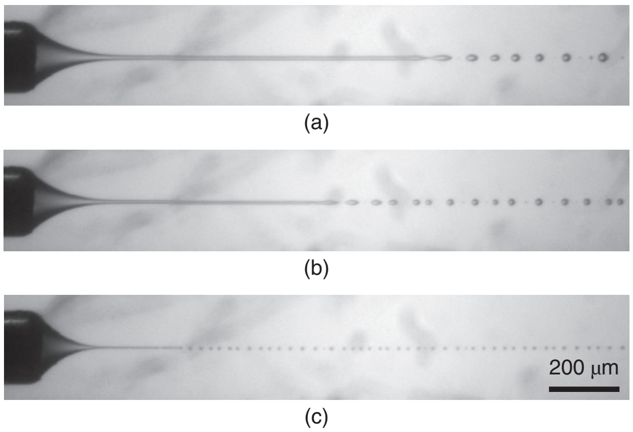

Figure 1.6 Experimental images showing jet formation and breakup when silicone oil of 10 cP is used as inner fluid and glycerin as the outer fluid. $\mu_i/\mu_o = 10^{-2}$ and $Ca_o = 5$. (a) $U_i/U_o = 10^{-2}$, $Q_i = 5 \times 10^{-1}$ μl/min, $Q_o = 7$ ml/min; (b) $U_i/U_o = 6 \times 10^{-3}$, $Q_i = 3 \times 10^{-1}$ μl/min, $Q_o = 7$ ml/min; (c) $U_i/U_o = 5 \times 10^{-4}$, $Q_i = 2 \times 10^{-2}$ μl/min, $Q_o = 7$ ml/min. Source: Reprinted Figure 2 from Ref. [31].

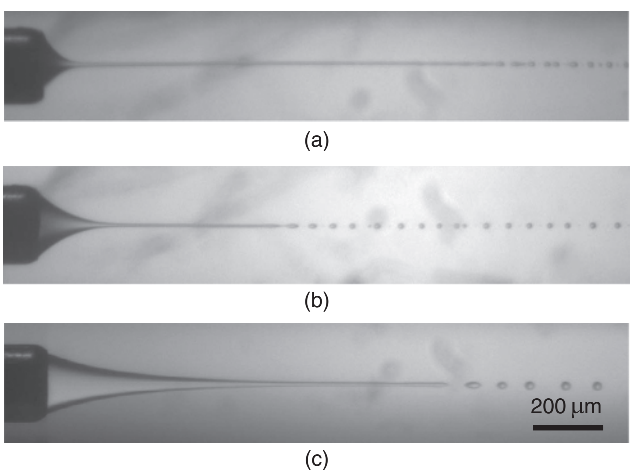

Figure 1.7 Experimental images showing jet formation and breakup for $Ca_o = 5$, $U_i/U_o = 4 \times 10^{-3}$ and different values of the viscosity ratio: (a) silicone oil of 100 cP/glycerin, $\mu_i/\mu_o = 10^{-1}$; (b) silicone oil of 10 cP/glycerin, $\mu_i/\mu_o = 10^{-2}$; (c) water/silicone oil of 1000 cP, $\mu_i/\mu_o = 10^{-3}$. $Q_i = 2 \times 10^{-2}$ μl/min, $Q_o = 7$ ml/min. Source: Reprinted Figure 6 from Ref. [31].

that result from its breakup both decrease (see Figure 1.6), consistent with the results shown in Fig. 1.5. In addition, when Ca_o reaches a value above the threshold at which the transition between dripping and jetting occurs, they reported that the length of the jet before breakup is proportional to Ca_o, whereas the jet diameter and, as a consequence, the droplet size remain constant. Lastly, they could verify that if the viscosity ratio decreases, the cone-jet structure becomes more elongated (see Figure 1.7), eventually resulting in

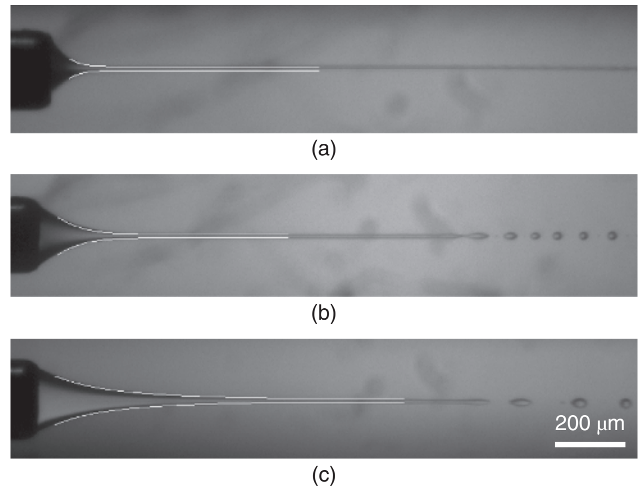

Figure 1.8 Experimental images obtained using different silicone oils as the inner fluid and glycerin as the outer fluid for $Ca_o = 5$. The continuous white line corresponds to the theoretical jet shape. The values of the control parameters in each of the three cases shown are (a) $\mu_i/\mu_o = 10^{-1}$, $U_i/U_o = 6 \times 10^{-3}$, $Q_i = 3 \times 10^{-1}$ μl/min, $Q_o = 7$ ml/min; (b) $\mu_i/\mu_o = 10^{-2}$, $U_i/U_o = 10^{-2}$, $Q_i = 5 \times 10^{-1}$ μl/min, $Q_o = 7$ ml/min; (c) $\mu_i/\mu_o = 10^{-3}$ $U_i/U_o = 10^{-2}$, $Q_i = 8 \times 10^{-1}$ μl/min, $Q_o = 12$ ml/min. Source: Reprinted Figures 18–20 from Ref. [32].

aperiodic jet breakup and a drop size that is no longer uniform.

Making use of the continuity equation, the axial momentum equation, the normal stress balance across the interface and the kinematic boundary condition at the free interface, they obtained a parameter-free theoretical prediction for the jet shape, finding good agreement with the experimental results (Figure 1.8).

1.2.4 Unified Scaling of the Drop Size in Both Narrowing and Widening Regimes

The drop size that results from the breakup of a widening jet decreases with Q_o for a fixed Q_i, consistent with the results for narrowing jets. In contrast, when Q_i is increased for a fixed value of Q_o, two different situations are observed: If the viscosity of the outer fluid is $\mu_o \simeq 10$ cP, the behavior of d_{drop} is consistent with the situation encountered with narrowing jets; d_{drop} increases with Q_i. However, when $\mu_o \simeq 1$ cP, the opposite behavior is observed and the drop size decreases with Q_i, as shown in Figure 1.9.

To understand this dependence, let us revisit the behavior of narrowing jets. Since for these jets, $Re_o < 1$, there is an effective diffusion of momentum across the whole cross section of the jet. As a result, the inner and outer velocities become equal at some distance downstream of the injection

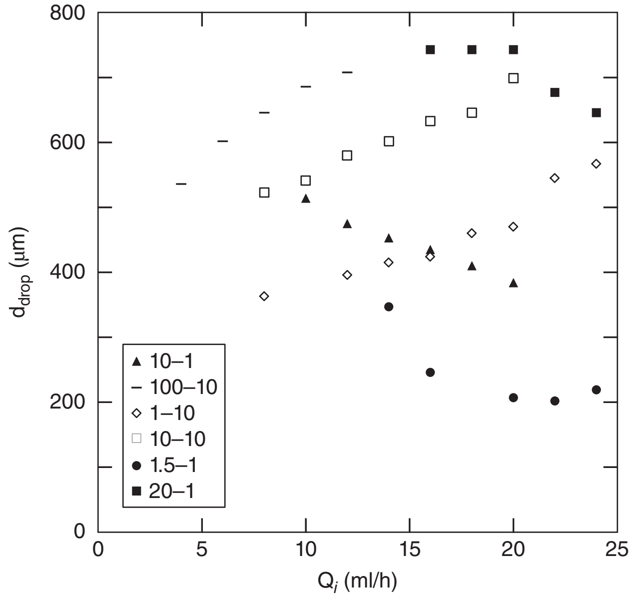

Figure 1.9 Dependence of the drop diameter on Q_i for a fixed value of $Q_o = 200$ ml/h and various inner/outer viscosities. Observe that the trends are different depending on the values of the inner and outer viscosities. Numbers in the caption indicate inner/outer viscosities in centipoises. Source: Reprinted Figure 7c from Ref. [26].

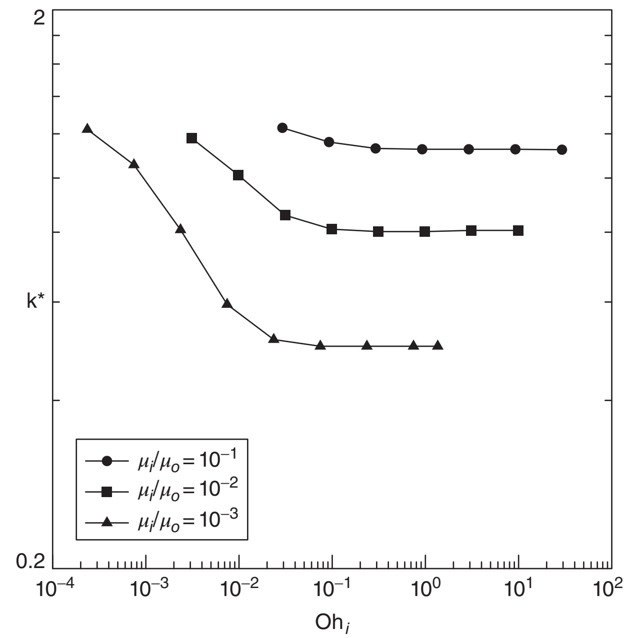

Figure 1.10 Dimensionless wave number versus inner Ohnesorge number for different viscosity ratios.

tube and the jet diameter simply results from

$$\frac{\pi d_{\text{jet}}^2}{4} U_o = Q_i \to d_{\text{jet}} = \left(\frac{4Q_i}{\pi U_o}\right)^{1/2}, \tag{1.2}$$

which is consistent with Equation 1.1 for $d_{\text{jet}} \ll D_o$, except for a numerical prefactor related to the details of the velocity profile. In addition, since these jets are convectively unstable (see Section 2.5), the size of the drops obtained from their breakup can be determined from the mass balance: $\pi\, d_{\text{drop}}^3/6 = \pi^2 d_{\text{jet}}^3/(4k^*)$, where $k^* = k^*(\mu_i/\mu_o, Oh_i)$ is the dimensionless wave number corresponding to the maximum growth rate of sinusoidal capillary perturbations and $\lambda^* = \pi d_{\text{jet}}/k^*$ is its corresponding wavelength. Since k^* depends weakly on Oh_i for relatively large values of this parameter, as shown in Figure 1.10, it is sensible to write $k^* = k_t^*$, with $k_t^* = k_t^*(\mu_i/\mu_o)$ the dimensionless wave number corresponding to the maximum growth rate in the limit, first considered by Tomotika [29], $Oh_i \to \infty$. With these considerations and using Equation 1.2 , we obtain

$$d_{\text{drop}} = \left(\frac{144}{\pi}\right)^{1/6} (k_t^*)^{-1/3} \left(\frac{Q_i}{U_o}\right)^{1/2}. \tag{1.3}$$

Castro-Hernández *et al.* [27] extended these ideas to describe the behavior of d_{drop} for both narrowing and widening jets. The main quantity in this approach is the time for drop formation, T, which is the sum of the convective time, t_{conv}, and the pinch-off time, t_{pinch}: $T = t_{\text{conv}} + t_{\text{pinch}}$ [33]. The convective time, t_{conv}, is the time required to convect the inner fluid a distance λ at a velocity U_p, where λ is the distance traveled by the downstream location of the jet within two consecutive pinch-off events and U_p is the velocity of the tip of the jet, as shown in Figure 1.11. The pinch-off time is the time needed to break the liquid thread. Since $t_{\text{pinch}} \ll t_{\text{conv}}$ in most experimental situations, breakup can be considered to take place almost instantaneously. However, for breakup to happen, a length equal to $\lambda^* = \pi d_{\text{jet}}/k^*$ is required. This means that the downstream location of the jet would need to travel a distance λ^* before breakup can occur. As a result,

$$T = \frac{\lambda}{U_p} = \frac{\pi\, d_{\text{jet}}}{k^*\, U_p}, \tag{1.4}$$

and since continuity demands that $\pi d_{\text{drop}}^3/6 = Q_i T$, then

$$\frac{d_{\text{drop}}}{D_i} = \frac{1}{D_i}\left(\frac{6\, Q_i\, d_{\text{jet}}}{k^*\, U_p}\right)^{1/3}. \tag{1.5}$$

The drop diameter is then determined by d_{jet}, k^*, and U_p. For the narrowing jets, $U_p \simeq U_o$ [24] and Equation 1.5 corresponds to Equation 1.3 . However, for the widening jets, this is not always the case. If the outer fluid viscosity is large compared to the viscosity of water, $U_p \simeq U_o$ and Equation 1.5

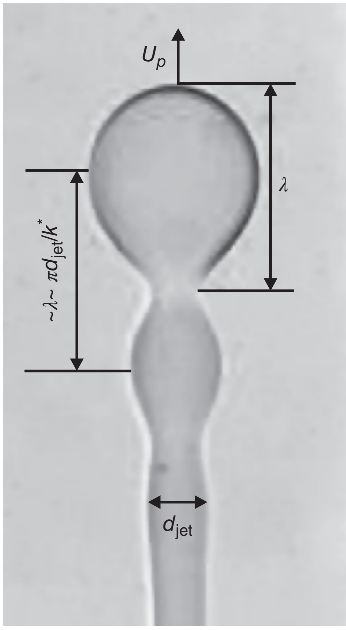

Figure 1.11 Image showing the velocity at the more downstream position of the jet, U_p, the jet diameter, d_{jet}, and the axial distance traveled by the tip of the jet between two consecutive pinch-off events, λ. The value of λ can be approximated by the wavelength corresponding to the maximum growth rate of capillary perturbations, $\pi d_{jet}/k^*$. Source: Reprinted Figure 8 from Ref. [26].

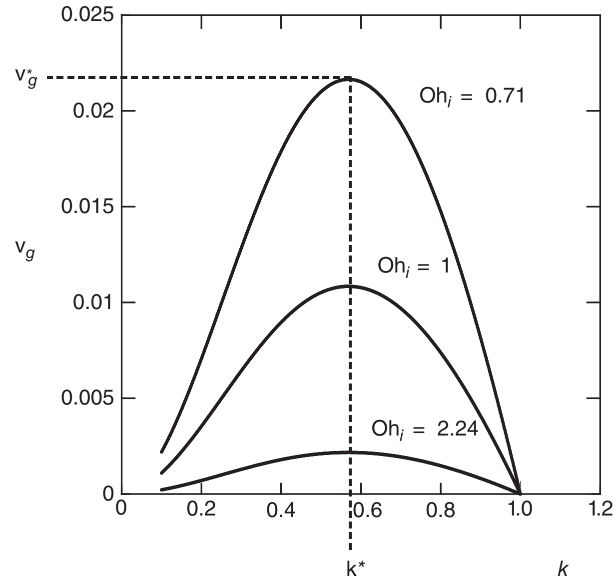

Figure 1.12 Growth rate, v_g, versus dimensionless wave number for different values of the inner Ohnesorge number and $\mu_i/\mu_o = 0.1$. Source: Reprinted Figure 11 from Ref. [26].

captures the increase of d_{drop} with Q_i observed experimentally. In contrast, when the outer viscosity is similar to that of water, $U_p \neq U_o$ since the inner fluid can drag the outer fluid and affect the velocity of the jet interface, which will then be larger than the outer velocity. As a result, $U_p = f(Q_i)$ and could result in a decreasing d_{drop} with Q_i. See [27] for further details.

This is not the only difference between narrowing and widening jets. As we have seen, the jet diameter for the case of the narrowing jets is simply $d_{jet} = [4Q_i/(\pi U_o)]^{1/2}$ [24, 31]. However, for the widening jets this equality is generally not correct since the inner liquid velocity can be different from U_o, as pointed out in the previous paragraph. Hence, a different way to estimate d_{jet} is needed. To do this, we recall that upstream the breakup point, this inner liquid velocity is larger than the speed of capillary perturbations; this explains why the jets do not break in this region. As the jet widens downstream, the inner liquid velocity decreases and at some axial location, it becomes comparable to the speed of capillary disturbances. At this place, the jet breaks. We emphasize that this can happen before the inner velocity of the jet equals the outer fluid velocity. Based on this, we estimate d_{jet} from the condition $t_{pinch} \simeq t_{prop}$, where t_{prop} is a characteristic time for the propagation of capillary perturbations, $t_{prop} = d_{jet}/U_i$, with $U_i = 4Q_i/(\pi d_{jet}^2)$. The characteristic pinch-off time is $t_{pinch} = 1/(v_g^*)(\rho_i/\mu_i)\,(d_{jet}/2)^2$, with v_g^* the maximum dimensionless growth rate associated to k^* (see Figure 1.12). With all these facts, we obtain

$$d_{jet} = \frac{1}{v_g^*}\frac{\rho_i Q_i}{\pi \mu_i}, \tag{1.6}$$

Taking all these aspects into account, we consider the data in Figure 1.9 together with the drop size data of narrowing jets and plot d_{drop}/D_i versus $[6Q_i d_{jet}/(k^* U_p)]^{1/3}/D_i$, where d_{jet} is obtained from Equation 1.6 and U_p is taken equal to U_o when $\mu_o \geq 5$ cP or it is directly measured experimentally. For k^*, we solve Tomotika's complete equations for any value of Oh_i; see Ref [29]. We find that there is a linear relation between the two quantities, as shown in Figure 1.13 and consistent with the expectations from Equation 1.5 . Furthermore, the slope of the best fit is 0.9, which is close to 1, and the intercept is 0.75, which is small compared to the values of d_{drop}/D_i. Thus, the proposed model correctly describes the drop size that results from the breakup of both widening and narrowing jets.

1.2.5 Convective Versus Absolute Instabilities

Dripping is a common example of an absolute instability, where the perturbations that induce breakup grow in time at a fixed location in space, at a frequency that is intrinsic to the system. As a result, dripping is insensitive to external noise and results in extremely monodisperse droplets. By contrast, jetting is often the result of a convective instability, where

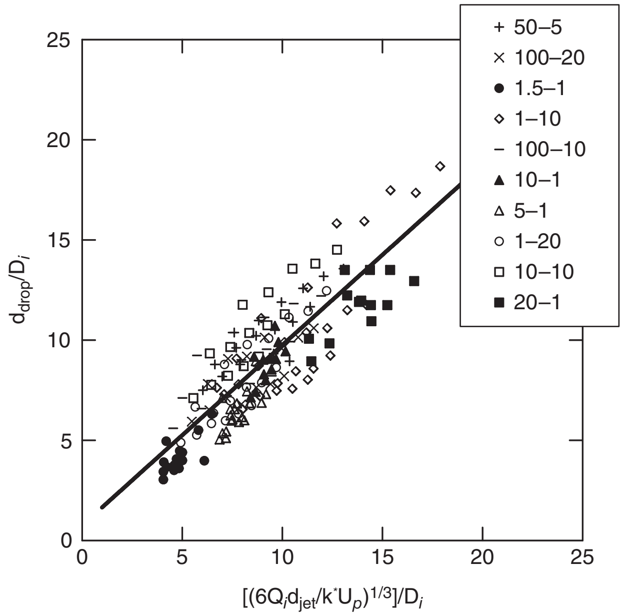

Figure 1.13 Experimentally measured drop diameters d_{drop}/D_i as a function of the parameter $(6\,Q_i\ d_{\mathrm{jet}}/(D_i^3\ k^*\ U_p))^{1/3}$. The slope of the linear regression fit to the experimental data is very close to 1, consistent with the theoretical prediction given by Equation (1.5). The relative errors, however, are ±30%. The maximum experimental error associated to the measurement of the tip velocity is of the order of ∼ 10%. Hence, the dispersion in the data is attributable to necessary simplifications in the way the wavelength of maximum growth rate and the tip velocity, U_p, are calculated. Numbers in the caption indicate inner/outer viscosities in centipoises. Source: Reprinted Figure 13b from Ref. [26].

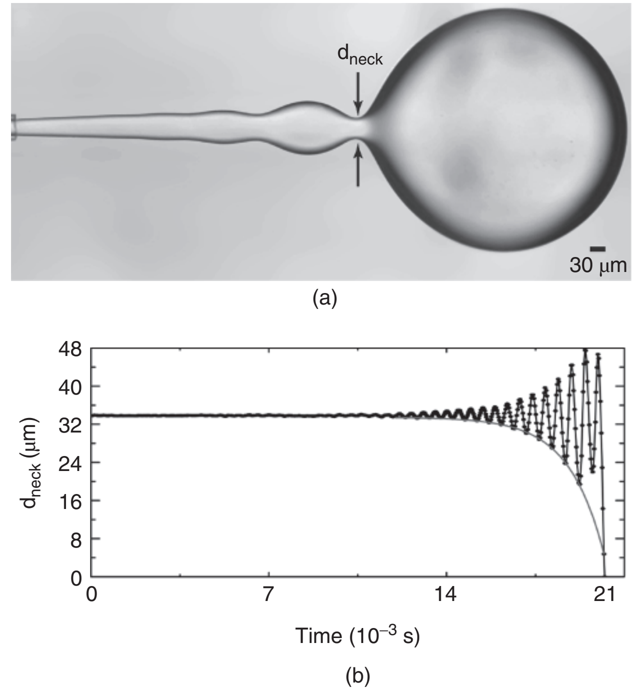

Figure 1.14 (a) High-speed image of a typical widening jet. The small neck between the jet and the bulb has a diameter, d_{neck}. The outer diameter of the tip is ∼ 40 μm, while $d_{\mathrm{tip}} \simeq 30$ μm and the inner diameter of the surrounding cylindrical capillary is ∼ 600 μm. Here $We_i = 5.5$. (b) Neck diameter as a function of time. The line is an exponential fit to the envelope. The associated growth rate is ∼ 40 Hz. The frequency of oscillation is ∼ 2000 Hz. The flow rates of the outer and inner fluids are 9×10^4μl/h and 6×10^3μl/h, respectively. Source: Reprinted Figure 1 from Ref. [32]. Copyright 2008 by the American Physical Society.

the perturbation that leads to breakup amplifies the external noise as it is advected downstream, usually leading to less uniform droplets.

Absolute instabilities in the jetting regime are rarely observed. However, Utada *et al.* [34] reported that drop formation in the widening jet regime happens via absolute, rather than convective instabilities. Experimentally, this is supported by the following facts: (i) Despite the widening jets are generated by injecting the inner fluid at $We_i > O(1)$, drop pinch-off from the end of the jet occurs only after the jet diameter has widened sufficiently such that We_i decreases to order unity as in the dripping regime, which only occurs when $We_i \lesssim O(1)$ and results in drop formation via absolute instabilities [35, 36]. (ii) The large difference in velocity between U_i and the neck of the widening jet, highlighted with arrows in Figure 1.14(a), coupled with the spatially stationary oscillations throughout the entire pinch-off process suggests that the superposition of the perturbations produces the condition of zero group velocity at a fixed location. (iii) The envelope associated to the oscillatory motion of the neck grows exponentially in time, as shown in Figure 1.14(b) for the case of $\mu_i/\mu_o = 0.1$, implying that the growth rate of the instability is positive.

Narrowing jets essentially break via Rayleigh-Plateau instabilities that are convected by the flow. Nevertheless, assessing whether widening jets indeed result from absolute instabilities requires performing a linear stability analysis. Using the classical quasi-parallel approximation, any parameter associated with the flow, such as the velocity and the pressure, is assumed to be proportional to exp $(\mathrm{i}(kz - wt))$, where z is the axial position measured with respect to the injection needle and t is the time. In general, the frequency, $w = w_r + \mathrm{i}w_i$, and the wave number, $k = k_r + \mathrm{i}k_i$, are complex and are related through a dispersion relation $D(\omega, k) = 0$. Furthermore, the superposition of all possible modes generates wave packets that travel both up- and downstream along the interface of the jet with group velocity $v_g = \partial w_r/\partial k_r$. Typically, a temporal stability analysis is used to determine whether or not a system is stable.

This corresponds to examining the behavior of the perturbations over time. In this analysis, the wave number is assumed to be real and the frequency is a complex quantity. If the growth rate of the instability is negative, $\omega_i < 0$, the perturbations decay in time, the jet is temporally stable and breakup will not occur. In contrast, if $\omega_i > 0$, the perturbations grow exponentially in time, the jet is temporally unstable and breakup can occur. The breakup time of the jet is calculated from the growth rate, $t_b = 1/\omega_i$ and the drop size can be determined from $Q_i t_b = \pi d_{\mathrm{drop}}^3/6$.

For the unstable situations in the temporal analysis, we perform an additional spatiotemporal study to distinguish absolute from convective instabilities. This analysis is based on the Briggs–Bers criterion [37, 38], which is employed to determine whether perturbations introduced at a fixed spatial location in the flow are amplified or decay at that spatial location. For that purpose, we look for frequencies and wave numbers, ω_0 and k_0, that satisfy the dispersion relation, $D(\omega_0, k_0) = 0$, and result in a zero group velocity, $v_g|_{\omega=\omega_0,k=k_0} = 0$ at some specific spatial location, in the laboratory frame of reference. If $\mathrm{Im}(\omega_0) < 0$, the instability is convective since the perturbations decay in time at that specific spatial location. In contrast, if $\mathrm{Im}(\omega_0) > 0$, the instability is absolute since the perturbations grow exponentially in time at that spatial location. When the instability is convective, unstable waves are convected in the direction of the flow. In this case, what one visually sees is the result of an unperturbed flow with superimposed waves that grow and propagate in the downstream direction. If, however, the instability is absolute, the stability analysis predicts that tiny perturbations will exponentially grow in time right at the place where the noise is introduced, preventing the unperturbed flow to be experimentally observable. In this way, whether the instability is convective or absolute can be detected experimentally.

The simplest stability analysis is the parallel stability analysis, which consists in solving the stability problem at every spatial location of the base flow, once it is assumed that, as far as the stability problem is concerned, the velocity profile at such axial location remains unchanged in the downstream and upstream directions up to $\pm\infty$, respectively. Interestingly, this approach correctly captures the differences observed experimentally in the resulting flow [34, 39]. For this reason, despite a global stability analysis [40, 41] would be conceptually more appropriate to predict what is experimentally observed, in this section we only present results obtained with the local parallel flow assumption.

To perform the stability analysis under the parallel flow assumption, we need to know the steady base flow. Hence, we need to calculate the downstream evolution of the velocity profiles of both inner and outer fluids. These can be obtained from the continuity and Navier–Stokes equations, which in the slender jet approximation can be written as [42]

$$\frac{\partial u^{i,o}}{\partial z} + \frac{1}{r}\frac{\partial (r v^{i,o})}{\partial r} = 0, \tag{1.7}$$

$$u^{i,o}\frac{\partial u^{i,o}}{\partial z} + v^{i,o}\frac{\partial u^{i,o}}{\partial r} = \nu^{i,o}\frac{1}{r}\frac{\partial}{\partial r}\left(r\frac{\partial u^{i,o}}{\partial r}\right) - \frac{1}{\rho^{i,o}}\frac{\partial P^{i,o}}{\partial z}, \tag{1.8}$$

where u and v are the axial and radial velocities, respectively, and the superscripts refer to outer and inner fluids, respectively. Once the system of equations above is solved subjected to the boundary conditions (see [42]), we find that the parabolic velocity profile of the inner fluid is very pronounced near the tip, as shown by the curve for $z = 36$ μm in Figure 1.15, and progressively flattens downstream, as shown by the curves for $z = 160$ μm, $z = 336$ μm, and $z = 513$ μm in Figure 1.15. In contrast, the velocity profile of the outer liquid is essentially flat on the length scale of the jet. We confirm that the local Weber number is of order unity at the experimental distance from the tip where jet breakup happens.

This base flow is then perturbed at each z to obtain the sign of the imaginary part of ω_0. The axial distance, z^*, where the instability transitions between convective and absolute, can be located studying the behavior of the solutions of the dispersion relation in the complex k-plane. These solutions can be seen as propagating wave packets with an amplitude that increases or decreases depending on whether they correspond to unstable or stable modes, respectively. The way to distinguish if these solutions represent upstream or downstream wave packets is by noting the sign of the group velocity. If $v_g > 0$, the wave packet travels downstream, while if $v_g < 0$, the wave packet travels

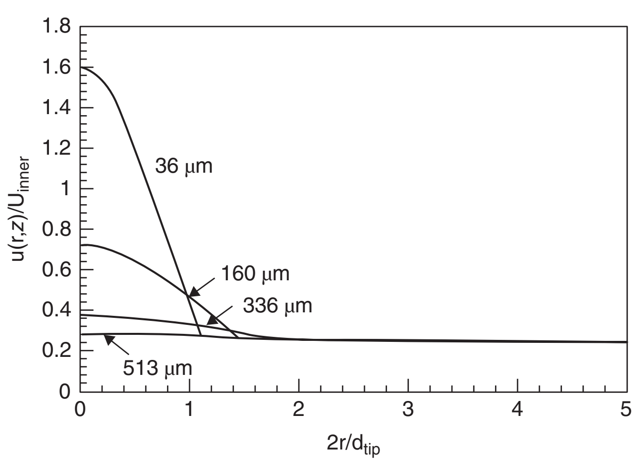

Figure 1.15 Velocity profile for different axial positions. The parameters used in this case are $\mu_i/\mu_o = 0.1$, $We_i = 1.66$ and $Ca_o = 0.67$.

upstream. Now, since we are only interested in a local stability analysis, we can perform a Taylor expansion of $D(\omega, k)$ around (ω_0, k_0) and keep terms up to leading order in ω and k: $D(k, \omega) = D(k_0, \omega_0) + [\partial D(k, \omega)/\partial \omega]_{k_0,\omega_0}(\omega - \omega_0) + [\partial^2 D(k, \omega)/\partial k^2]_{k_0,\omega_0}(k - k_0)^2/2$, where we have used that $[\partial D(k, \omega)/\partial k]_{k_0,\omega_0} = [\partial D(k, \omega)/\partial \omega]_{k_0,\omega_0}[\partial \omega/\partial k]_{k_0,\omega_0} = 0$, given that the group velocity at (ω_0, k_0) is zero. In this case, the dependence between ω and k is quadratic, implying that, in the vicinity of (ω_0, k_0), there are two solutions; these correspond to wave packets propagating in opposite directions and appear as branches in the complex k-plane, as shown in Figure 1.16 for representative values of z. The value of z^* can then be located as the axial distance where the two branches coalesce. This corresponds to the existence of a saddle point in the complex k-plane. Mathematically, this means that at z^*: $D(\omega_0, k_0) = 0$, $[\partial D(\omega, k)/\partial k]_{\omega_0,k_0} = 0$, $\mathrm{Im}(\omega_0) = 0$ and $[\partial^2 D(\omega, k)/\partial k^2]_{k_0,\omega_0} \neq 0$.

The way to find the saddle point is equivalent to solving the so- called signaling problem [43] at every spatial location, for situations where the stable perturbations are convected upstream. Note first that the signaling problem consists in finding the response of the unperturbed flow to a periodic forcing of small amplitude. In the case of a stable flow, the amplitude of the perturbations will decay both in the upstream and downstream directions. In contrast, the flow will be convectively unstable if stable/unstable perturbations propagate in the upstream/downstream direction. When the conditions for a saddle point are fulfilled, the group velocity of unstable perturbations is zero, implying that the energy seeded in the flow by the forcing cannot be evacuated away from the location where it is introduced.

For the case of $\mu_i/\mu_o = 0.1$, $Ca_o = 0.67$, and $We_i = 1.66$, Utada et al. [34] find that this point is located at $z^* \approx 275$ μm. For $z < z^*$, $\mathrm{Im}(\omega_0) > 0$ and the instability is absolute, while for $z > z^*$, $\mathrm{Im}(\omega_0) < 0$ and the instability is convective. When the region of the jet located right at the exit of the injection tube that is absolutely unstable is much larger than the characteristic wavelength of the absolute mode, $\lambda_0 = 2\pi/k_0$, the jet breaks via an absolute instability. The transition to a convective instability takes place for the values of the Capillary and Weber numbers for which the extent of the region adjacent to the injector where the instability is absolute, either is zero, or possesses a length much smaller than that of the wavelength of the absolute mode.

As a further test to the interpretation of the experimental results, Utada et al. [34] did additional experiments to induce a transition from an absolute to a convective jet instability. The idea was to start with a jet that breaks up via absolute instabilities and increase Ca_o sufficiently to induce the formation of a narrowing jet, which breaks up convectively. To achieve larger values of the outer capillary number, they used a more viscous outer fluid and set $\mu_i/\mu_o = 0.01$. They

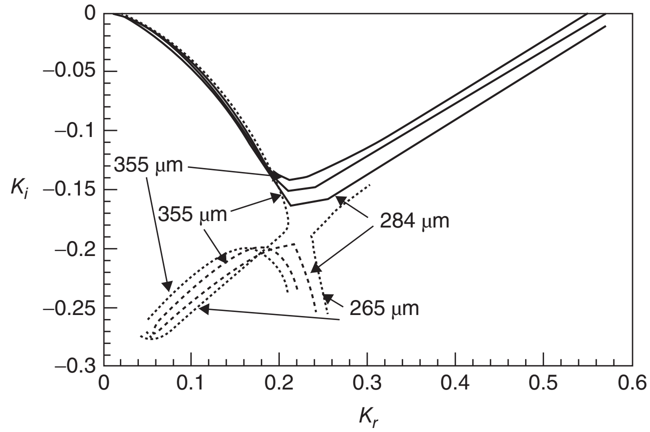

Figure 1.16 Saddle point in the complex k-plane indicating the axial location at which the instability transitions to absolute. The parameters used are $\mu_i/\mu_o = 0.1$, $We_i = 1.66$, and $Ca_o = 0.67$.

started with an absolutely breaking jet at $We_i = 3.1$ and $Ca_o < 1$ (see Figure 1.17a) and gradually increased Q_o and thus Ca_o. Interestingly, at a critical $Ca_o^* \simeq 0.65$, they observed an abrupt and dramatic increase in the length of the jet, as shown in Figure 1.17b–d. This large increase in the jet length also coincided with the suppression of the spatial oscillations that were observed initially, as also shown in Figure 1.17b and c. Remarkably, the stability analysis predicts that at $Ca_o^* = 0.69$ the instability transitions from absolute to convective, consistent with the experimental results. Furthermore, the theoretical analysis also predicts that Ca_o^* should not change significantly with We_i; this implies that the shear from the outer liquid determines the transition from an absolute to convective instability irrespective of the inertia of the inner liquid. This is remarkable because when $We_i < 1$ and $Ca_o < Ca_o^*$, the system is in a dripping regime; above Ca_o^*, however, the system transitions from an absolutely unstable dripping regime [36, 43–46] to a convectively unstable jetting one.

The experiments and their theoretical analysis then suggest that the widening jet regime results in drop formation via absolute instabilities, consistent with the dripping regime. In contrast, the narrowing jet regime results in drop formation via convective instabilities. The presence of absolute instabilities in jets then enables a route that is alternative to dripping for the generation of uniform emulsions. The key advantage here is that absolute instabilities are, in principle, not affected by noise.

1.3 FLOW FOCUSING

The flow focusing configuration can be implemented in an axisymmetric device [28, 48] or in a two- dimensional device that can be generated by soft-lithography techniques [49].

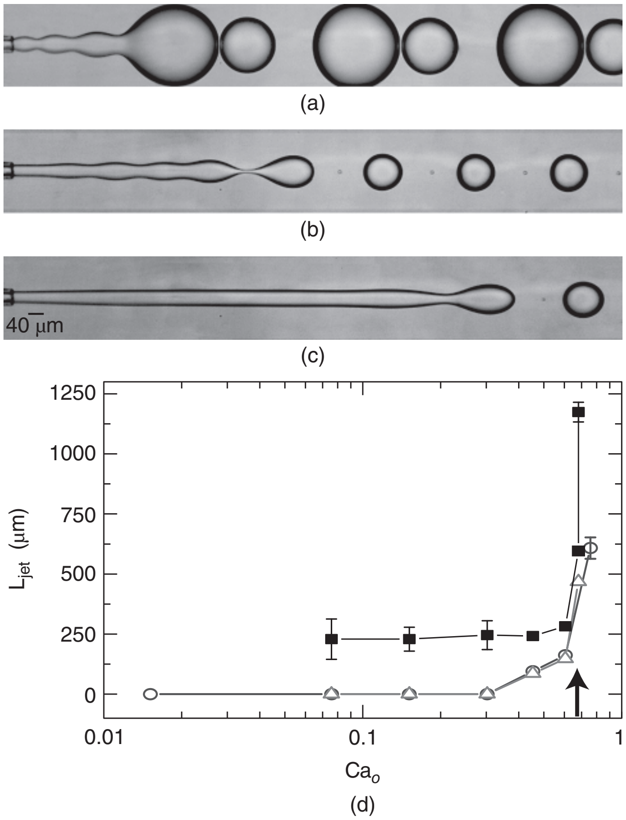

Figure 1.17 (a) Image of the jet generated at $We_i = 3.1$ and $Ca_o = 0.07$. (b) Transient image of the jet generated at $Ca_o = 0.69$. The oscillations on the jet gradually die out as the length increases at the critical value, Ca_o^*. (c) Image of the jet at $Ca_o = 0.69$ after the lengthening. (d) Plot of the jet length as a function of Ca_o. The filled squares are the measured jet lengths. The open circles and triangles are dripping. The We_i for the circles and triangles are 0.19 and 0.05, respectively. For these experiments, $\mu_i/\mu_o = 0.01$. Source: Reprinted Figure 3 from Ref. [32]. Copyright 2008 by the American Physical Society.

Different configurations are possible with an axisymmetric flow focusing device, as shown in Figure 1.18. Using a gas as focusing fluid and a liquid as focused stream in a simple configuration, the generation of a spray is observed. If the fluids are both liquids, this technique allows the generation of emulsions that may be used as templates to produce particles, for example, by means of an evaporative solvent method [50]. Using a concentric device where the immiscible fluids are focused by an outer stream, the production of capsules has also been reported [51].

In the simplest axisymmetric version, a fluid is injected through a needle of inner diameter D_i, which is in front of an orifice of diameter D, located at a distance H from the needle, surrounded by an outer immiscible fluid that focuses the inner stream through the orifice. As in the coflow configuration, a "dripping" mode and a jetting regime can be obtained. The "dripping" regime is characterized by the generation of droplets close to the orifice, within a distance of about one orifice diameter. By contrast, when jetting occurs, the droplets are produced at the end of a jet that extends at least three orifice diameters.

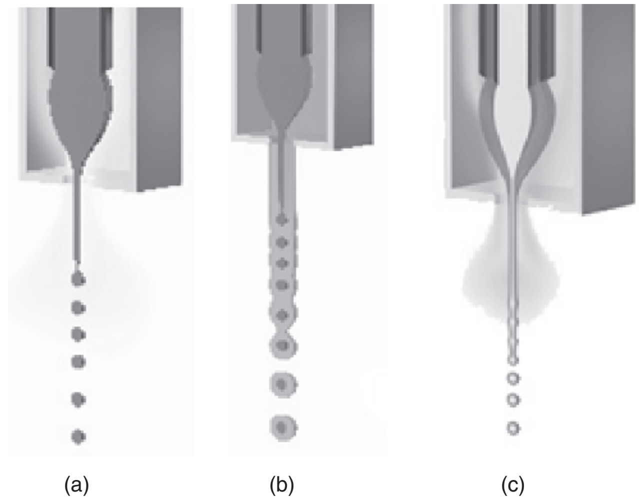

Figure 1.18 Different configurations in an axisymmetric flow focusing device. (a) Simple gas–liquid. (b) Simple liquid–liquid. (c) Concentric. Source: Reprinted Figure 21 from L. Martín-Banderas's PhD Thesis Reference [52].

When operated under adequate conditions, the inner stream can develop a cusp-like shape that is stable and that results in a thin jet of diameter d_{jet} that eventually breaks into droplets due to capillary instabilities. In these devices, the Weber and Reynolds numbers are generally much larger than one, which means that the process is essentially controlled by inertia.

The simple flow focusing configuration when the outer fluid is a gas and the focused stream is a liquid has been extensively described by Gañán-Calvo [48] when operated in the jetting regime. The physical properties involved in this problem are the density of the inner stream, ρ_i, its viscosity, μ_i, the inner flow rate, Q_i, the outer pressure drop, ΔP_o, the surface tension between both phases, σ, the diameter of the injection tube, the diameter of the orifice, and the distance between the capillary tube and the orifice. As the characteristic lengths are below the capillary length, gravitational forces are negligible.

Perhaps the most important quantity to control is the jet diameter, which is almost constant along the jet, or alternatively the jet velocity $U_{\text{jet}} = 4Q_i/(\pi d_{\text{jet}}^2)$. Using d_{jet} and U_{jet} as characteristic length and velocity, the Weber and Reynolds numbers based on the properties of the inner fluid are $We_i = \rho_i U_{\text{jet}}^2 d_{\text{jet}}/\sigma$ and $Re_i = \rho_i U_{\text{jet}} d_{\text{jet}}/\mu_i$. For large values of these numbers, surface tension and viscous effects can be neglected and it is possible to assume that the energy injected in the system is transformed into kinetic energy of

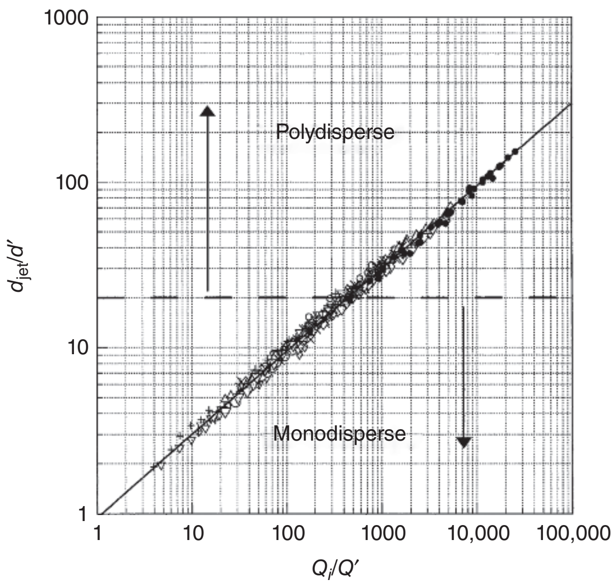

Figure 1.19 Dimensionless jet diameter at the constriction as a function of the nondimensional inner flow rate for different liquids and geometrical configurations. Source: Reprinted Figure 5 from Ref. [47]. Copyright 1998 by the American Physical Society.

the jet. This allows the estimation of the jet diameter [52]:

$$\Delta P_o \approx \frac{1}{2}\rho_i U_{\text{jet}}^2 \quad \Rightarrow \quad d_{\text{jet}} = \left(\frac{8\rho_i}{\pi^2 \Delta P_o}\right)^{\frac{1}{4}} Q_i^{1/2} . \qquad (1.9)$$

Another important quantity is the minimum liquid flow rate, for a given device and hence a given ΔP_o, resulting in a stable jet. This results from the requirement that $We_i = 1$, as otherwise jet formation would not be achieved. The result is $Q_{\text{min}} = (\sigma d_{\text{jet}}^3/\rho_i)^{1/2}$.

Measurements of d_{jet} for different liquids and geometrical configurations all collapse together in a single mastercurve when scaled by a reference length, $d' = \sigma/\Delta P_o$, and plotted versus a dimensionless inner-fluid flow rate, Q_i/Q', with $Q' = (\sigma^4/(\rho_i \Delta P_o)^3)^{1/2}$ (see Figure 1.19). This implies that

$$d_{\text{jet}}/d' = (8/\pi^2)^{1/4}(Q_i/Q')^{1/2} . \qquad (1.10)$$

Since μ_i is not a relevant quantity, there are seven variables and hence four independent dimensionless groups. Two of them have already been identified as d' and Q'. The other two can be chosen as D_i/D and H/D and involve geometrical details of the device. These are indeed important since for a chosen D_i, there is an optimum value of H for which Q_{min} is minimum. Moreover, this value significantly depends on D. As expected, then, if D_i is increased, H and D should increase accordingly to ensure similarity in the working conditions.

In flow focusing, both global and local instabilities are important. We say that flow focusing is globally unstable if a steady meniscus cannot be formed [18]. Three mechanisms responsible for global instability have been identified. (i) If d_{jet} is too small, the injected energy is invested in surface energy resulting in the lack of steady-state emission. (ii) When the applied pressure is not big enough, the stresses exerted by the outer stream on the jet interface do not overcome surface tension forces and the meniscus never forms. (iii) For small enough inner flow rates, recirculation cells are formed inside the meniscus preventing jet formation and ultimately interrupting the flow.

Importantly, global stability is a necessary but not a sufficient condition to obtain a stable jet. Flow focusing must also be locally stable, which means that the jet must be convectively unstable. As a consequence, the growing perturbations must be convected downstream and result in a steady liquid ligament. If the jet is absolutely unstable, "dripping" kicks in. Vega *et al.* [18] performed a stability analysis showing that the "dripping" to jetting transition can be described as a transition from an absolute to a convective instability. Hence, the "dripping" mode is associated to an absolutely unstable jet, while the jetting mode is associated to a convectively unstable jet.

Figure 1.20 shows the stability regions in the We_i, Re_i representation when water is used as focused fluid and air as focusing fluid with $H = D_i = 200$ μm. Three different regimes are observed: (i) the steady jetting regime, where the meniscus is stable and the jet is convectively unstable (jetting), (ii) the local instability regime, where the meniscus is stable and the jet is absolutely unstable (dripping), and (iii) the global instability regime, where the meniscus is unstable. The experimental data is plotted in the upper graph, while the lower graph reproduces the boundary lines seen experimentally and identifies the regions where these regimes are observed. The open symbols show transitions from steady states to local instability situations, while the solid symbols corresponds to transitions from local to absolutely unstable situations. The dotted line shows the prediction obtained from the linear stability analysis of the basic flow. The dashed-dotted line corresponds to $Q_{\text{min}} = 2.9$ ml/h for the fluids and device used in this particular experiment. Note that there is a turning point in the two experimental transition lines; above this point, as We_i increases, both lines almost coincide with the curve corresponding to a constant Q_{min}. Hence, there is a minimum value of the inner flow rate below which flow focusing becomes globally unstable independently of the outer pressure drop.

Vega *et al.* [52] perform the same stability analysis for different H/D and reported that the transition from the steady jetting mode to the locally unstable "dripping" mode was not affected by the geometry. The same conclusion was reached for the transition from local to global instability

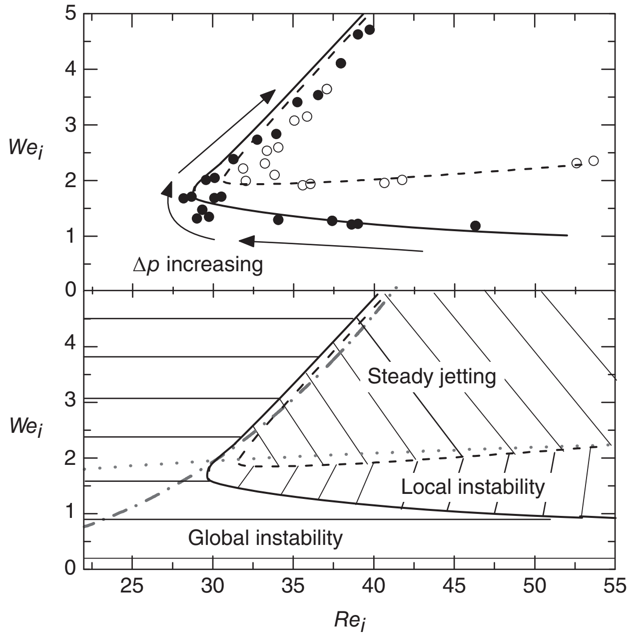

Figure 1.20 The lower graph shows the stability regions plotted from the experimental data shown in the upper graph. The dashed-dotted line is the curve of constant minimum flow rate, while the dotted line is the Leib and Goldstein prediction for the convective/absolute transition. Source: Reprinted Figure 6 from Ref. [52].

at small Weber numbers. In contrast, the geometry and the properties of the focused fluid have an effect on $Q_{\min}$ and on the pressure drop corresponding to the turning point of the transition curves. In addition, the relative importance of the global instability region is smaller when μ_i increases; in this case, an additional dimensionless group accounting for the relative influence of the viscous force must be considered.

1.4 SUMMARY AND OUTLOOK

We have discussed the generation of droplets with a narrow size distribution using coflowing fluids and flow focusing:

(1) In the coflow configuration, a fluid is injected through an injection tube in the presence of an immiscible fluid that flows in parallel. Depending on the operating conditions, two different regimes are obtained: dripping and jetting. In the “dripping” regime, extremely monodisperse droplets are generated at the tip of the capillary tube with a low production rate. In contrast, in the jetting regime less monodisperse droplets are obtained at the end of a long liquid ligament or jet, but at much higher production rates. Within the jetting regime, we find that the jet can either widen or narrow in the downstream direction. Despite these jets break into droplets via either absolute or convective instabilities, respectively, the drop size can be unified by a single scaling law.

(2) In the flow focusing configuration, a focused fluid is forced by an immiscible focusing fluid through a constriction. This configuration can be implemented in an axisymmetric or in a two-dimensional device. In the “dripping” regime, the generation of the droplets occurs close to the orifice while in the jetting regime it happens within a distance at least three orifice diameters. We have reviewed the relevant scaling laws for the jet size and hence for the resulting drop size. In addition, we have discussed the operating regimes in terms of global and local instabilities, as well as in terms of absolute and convective instabilities.

The advantage of these techniques and the many related techniques that are currently in use or under development compared to the more traditional methods for emulsion generation rests on the exquisite fluid flow control offered by microfluidics. The high throughout is still the major hurdle for these techniques to completely dominate the field of emulsion generation.

REFERENCES

[1] Basaran OA. Small-scale free surface flows with break-up: drop formation and emerging applications. AIChE J 2002;48:1842.

[2] Squires TM, Quake SR. Microfluidics: fluid physics at the nanoliter scale. Rev Mod Phys 2005;77:977.

[3] Stone HA, Adjari A. Engineering flows in small devices: microfluidics toward a lab-on-a-chip. Annu Rev Fluid Mech 2004;36:381.

[4] Gunther A, Jensen KF. Multiphase microfluidics: from flow characteristics to chemical and materials synthesis. Lab Chip 2006;6:1487.

[5] Barrero A, Loscertales IG. Micro- and nanoparticles via capillary flows. Annu Rev Fluid Mech 2007;39:89.

[6] Clift R, Grace JR, Weber ME. *Bubbles, Drops, and Particles*. Mineola (NY): Dover Publications, Inc.; 2005.

[7] Liu H. *Science and Engineering of Droplets: Fundamentals and Applications*. Norwich (NY): William Andrew; 1999.

[8] Zúñiga RN, Aguilera JM. Aerated food gels: fabrication and potential applications. Trends Food Sci Technol 2008;19:176.

[9] Williams PA, Phillips GO, editors. *Gums and Stabilisers for the Food Industry 17: The Changing Face of Food Manufacture: The Role of Hydrocolloids*. Volume 346. Cambridge: The Royal Society of Chemistry; 2014.

[10] Martin-Banderas L. New trends in micro-and nano-systems development for pharmaceutical actives release. Med Chem (Shariqah (United Arab Emirates)) 2012;8(4):515.

[11] Michalet XEA. Quantum dots for live cells, in vivo imaging, and diagnostics. Science 2005;307:538.

[12] Gouin S. Microencapsulation: industrial appraisal of existing technologies and trends. Trends Food Sci Technol 2004;15:330.

[13] Friberg S, Jones S, Kroschwitz S. *Kirk-Othmer Encyclopedia of Chemical Technology*. 4th ed., Volume 9. New York: John Wiley and Sons; 1994.

[14] Kentish S, Simons L. The use of ultrasonics for nanoemulsion preparation. Innovative Food Sci Emerg Technol 2008;9(2):170.

[15] Yamada M, Seki M. Hydrodynamic filtration for on-chip particle concentration and classification utilizing microfluidics. Lab Chip 2005;5(11):1233–1239.

[16] Bhagat AAS, Kuntaegowdanahalli SS, Papautsky I. Inertial microfluidics for continuous particle filtration and extraction. Microfluid Nanofluid 2009;7(2):217–226.

[17] Shah RK, Shum HC, Rowat AC, Lee D, Agresti JJ, Utada AS, Chu L, Kim WK, Fernández-Nieves A, Martínez CJ, Weitz DA. Designer emulsions using microfluidics. Mater Today 2008;11(4):18–27.

[18] Vega EJ, Montanero JM, Herrada MA, Ga nán Calvo AM. Global and local instability of flow focusing: the influence of the geometry. Phys Fluids 2010;22(6):064105.

[19] Garstecki P, Fuerstman MJ, Stone HA, Whitesides GM. Formation of droplets and bubbles in a microfluidic T-junctions scaling and mechanism of break-up. Lab Chip 2006;6:437–446.

[20] Teh S, Lin R, Hung L, Lee AP. Droplet microfluidics. Lab Chip 2007;8:198–220.

[21] Christopher GF, Anna SL. Microfluidic methods for generating continuous droplets streams. J Phys D Appl Phys 2007;40:319–336.

[22] Vaschy A. Sur les lois de similitude en physique. Ann Télégraphiques 1892;19:25.

[23] Buckingham E. On physically similar systems. Illustrations of the use of dimensional equations. Phys Rev 1914;4:345.

[24] Utada AS, Fernández-Nieves A, Stone HA, Weitz D. Dripping to jetting transitions in co-flowing liquid streams. Phys Rev Lett 2007;99:094502.

[25] Rayleigh WS. On the capillary phenomena of jets. Proc Lond Math Soc 1879;29:71–97.

[26] Plateau J. Statique experimentale et theorique des liquides soumis aux seules forces moleculaires. Acad Sci Bruxelles Mem 1849;23:5.

[27] Castro-Hernández E, Gundabala V, Fernández-Nieves A, Gordillo JM. Scaling the drop size in coflow experiments. New J Phys 2009;11(7):075021.

[28] Utada AS, Lorenceau E, Link DR, Kaplan PD, Stone HA, Weitz D. Monodisperse double emulsions generated from a microcapillary device. Science 2005;308:537–541.

[29] Tomotika S. On the instability of a cylindrical thread of a viscous liquid surrounded by another viscous fluid. Proc R Soc A 1935;150:322–337.

[30] Suryo R, Basaran O. Tip streaming from a liquid drop forming from a tube in a co-flowing outer fluid. Phys Fluids 2006;18:082102.

[31] Marín AG, Campo-Cortés F, Gordillo JM. Generation of micron-sized drops and bubbles through viscous coflows. Colloids Surf A Physicochem Eng Aspects 2009;344:2–7.

[32] Castro-Hernández E, Campo-Cortés F, Gordillo JM. Slender-body theory for the generation of micrometre-sized emulsions through tip streaming. J Fluid Mech 2012; 698:423.

[33] Gordillo JM, Sevilla A, Martínez-Bazán C. Bubbling in a coflow at high Reynolds numbers. Phys Fluids 2007;19:077102.

[34] Utada AS, Fernández-Nieves A, Gordillo JM, Weitz D. Absolute instability of a liquid jet in a coflowing stream. Phys Rev Lett 2008;100:014502.

[35] Clanet C, Lasheras JC. Transition from dripping to jetting. J Fluid Mech 1999;383:307.

[36] Ambravaneswaran B, Subramani HJ, Philips SD, Basaran OA. Dripping-jetting transitions in a dripping faucet. Phys Rev Lett 2004;93:034501.

[37] Briggs RJ. *Electron Stream Interaction with Plasmas*. Cambridge (MA): MIT Press; 1964.

[38] Bers A. *Space Time Evolution of Plasma Instabilities*. Amsterdam: North Holland; 1983. p 451–517.

[39] Sevilla A, Gordillo JM, Martínez-Bazán C. Bubble formation in a coflowing air–water stream. J Fluid Mech 2005;530:181.

[40] Rubio-Rubio M, Sevilla A, Gordillo JM. On the thinnest steady threads obtained by gravitational stretching of capillary jets. J Fluid Mech 2013;729:471–483.

[41] Gordillo JM, Sevilla A, Campo-Cortes F. Global stability of stretched jets: conditions for the generation of monodisperse micro-emulsions using coflows. J Fluid Mech 2014;738:335–357.

[42] Gordillo JM, Pérez-Saborid M, Gañán Calvo AM. Linear stability of co-flowing liquid-gas jets. J Fluid Mech 2001; 448:23.

[43] Gordillo JM, Perez-Saborid M. Transient effects in the signaling problem. Phys Fluids 2002;14:4329.

[44] Gordillo JM, Gañán Calvo AM, Pérez-Saborid M. Monodisperse microbubbling: absolute instabilities in coflowing gas–liquid jets. Phys Fluids 2001;13:3839.

[45] Sevilla A, Gordillo JM, Martínez-Bazán C. Transition from bubbling to jetting in a coaxial air–water jet. Phys Fluids 2005;17:018105.

[46] Gañán Calvo AM, Riesco-Chueca P. Jetting–dripping transition of a liquid jet in a lower viscosity co-flowing immiscible liquid: the minimum flow rate in flow focusing. J Fluid Mech 2006;553:75.

[47] Guillot P, Colin A, Utada AS, Ajdari A. Stability of a jet in confined pressure-driven biphasic flows at low Reynolds numbers. Phys Rev Lett 2007;99:104502.

[48] Gañán Calvo AM. Generation of steady liquid microthreads and micron-size monodisperse sprays in gas streams. Phys Rev Lett 1998;80(2):285–288.

[49] Anna SL, Bontoux N, Stone HA. Formation of dispersions using Flow Focusing in microchannels. Appl Phys Lett 2003;82:364–366.

[50] Martín-Banderas L, Rodríguez-Gil A, Cebolla A, Chávez S, Berdún-Álvarez T, Flores-Mosquera M, Gañán Calvo AM. Towards high-throughput production of uniformly encoded microparticles. Adv Mater 2006;18(5):559–564.

[51] Gañán Calvo AM, Chávez S, Cebolla A, Flores-Mosquera M, Castro-Hernández E. Method of preparing micro and nanometric particles with labile products. PCT/ES2006/000212. 2009.

[52] Martín-Banderas L. Microencapsulación mediante la tecnología Flow-Focusing para aplicaciones biotecnológicas y biomédicas [PhD thesis]. Sevilla: CRAI Antonio Ulloa. Facultad de Farmacia, Universidad de Sevilla; 2007.